AGU PUBLICATIONS

Journal of Advances in Modeling Earth Systems

RESEARCH ARTICLE
10.1002/2015MS000477

Tropical cyclone flow asymmetries induced by a uniform flow revisited

Gerald L. Thomsen[1], Roger K. Smith[1], and Michael T. Montgomery[2]

[1]Meteorological Institute, Ludwig-Maximilians University of Munich, Munich, Germany, [2]Department of Meteorology, Naval Postgraduate School, Monterey, California, USA

Key Points:
- A uniform flow can organize inner-core convection
- An ensemble approach is used to address the stochastic nature of convection
- Our results raise significant questions about some previous theoretical work

Correspondence to:
M. T. Montgomery,
mtmontgo@nps.edu

Citation:
Thomsen, G. L., R. K. Smith, and M. T. Montgomery (2015), Tropical cyclone flow asymmetries induced by a uniform flow revisited, *J. Adv. Model. Earth Syst.*, *7*, 1265–1284, doi:10.1002/2015MS000477.

Received 8 MAY 2015
Accepted 20 JUN 2015
Accepted article online 14 JUL 2015
Published online 25 AUG 2015

Abstract We investigate the hypothesized effects of a uniform flow on the structural evolution of a tropical cyclone using a simple idealized, three-dimensional, convection-permitting, numerical model. The study addresses three outstanding basic questions concerning the effects of moist convection on the azimuthal flow asymmetries and provides a bridge between the problem of tropical cyclone intensification in a quiescent environment and that in vertical shear over a deep tropospheric layer. At any instant of time, explicit deep convection in the model generates flow asymmetries that tend to mask the induced flow asymmetries predicted by the dry, slab boundary layer model of Shapiro, whose results are frequently invoked as a benchmark for characterizing the boundary layer-induced vertical motion for a translating storm. In sets of ensemble experiments in which the initial low-level moisture field is randomly perturbed, time-averaged ensemble mean fields in the mature stage show a coherent asymmetry in the vertical motion rising into the eyewall and in the total (horizontal) wind speed just above the boundary layer. The maximum ascent occurs about 45° to the left of the vortex motion vector, broadly in support of Shapiro's results, in which it occurs ahead of the storm, and consistent with one earlier more complex numerical calculation by Frank and Ritchie. The total wind asymmetry just above the boundary layer has a maximum in the forward right sector, which is in contrast to the structure effectively prescribed by Shapiro based on an inviscid dry symmetric vortex translating in a uniform flow where, in an Earth-relative frame, the maximum is on the right.

1. Introduction

The predictability of tropical-cyclone intensification in a three-dimensional numerical model was investigated by *Nguyen et al*. [2008, henceforth M1]. They focused on two prototype problems for intensification, which consider the evolution of a prescribed, initially cloud-free, axisymmetric, baroclinic vortex over a warm ocean on an *f*-plane or β-plane. A companion study of the same problems using a minimal three-dimensional model was carried out by *Shin and Smith* [2008]. Both studies found that on an *f*-plane, the flow asymmetries that develop are highly sensitive to the initial low-level moisture distribution. When a random moisture perturbation is added in the boundary layer at the initial time, even with a magnitude that is below the accuracy with which moisture is normally measured, the pattern of evolution of the flow asymmetries is dramatically altered and no two such calculations are alike in detail. The same is true also of calculations on a β-plane, at least in the inner-core region of the vortex, within 100–200 km from the center. Nevertheless, the large-scale β-gyre asymmetries in that case are similar in each realization and as a result they remain when one calculates the ensemble mean. The implication is that the inner-core asymmetries on the *f* and β-plane result from the onset of deep convection in the model and, like deep convection in the atmosphere, they have a degree of randomness, being highly sensitive to small-scale inhomogeneities in the low-level moisture distribution. Such inhomogeneities are a well-known characteristic of the real atmosphere [e.g., *Weckwerth*, 2000].

In the foregoing flow configurations, there was no ambient flow and an important question remains: could the imposition of a uniform flow or a vertical shear flow lead to an organization of the innercore convection, thereby making its distribution more predictable? For example, there is evidence from observations [*Kepert*, 2006a, 2006b; *Schwendike and Kepert*, 2008] and from steady boundary layer models with varying degrees of sophistication that a translating vortex produces a coherent asymmetric pattern of low-level convergence and vertical motion [*Shapiro*, 1983; *Kepert*, 2001; *Kepert and Wang*, 2001]. However, the predicted asymmetries

from the steady boundary layer models differ significantly from each other. There is much evidence also that vertical shear induces an asymmetry in vortex structure [*Raymond*, 1992; *Jones*, 1995, 2000; *Smith et al*., 2000; *Frank and Ritchie*, 1999, 2001; *Reasor et al*., 2004; *Corbosiero and Molinari*, 2002, 2003; *Riemer et al*., 2010, 2013; *Reasor and Montgomery*, 2015].

An alternative question to that posed above is whether the flow asymmetries predicted by dry, steady boundary layer models survive in the presence of transient deep convection? The answer is not obvious to us since such models tacitly assume that the convection is able to accept whatever pattern and strength of upward vertical motion the boundary layer determines at its top and that it does not produce flow asymmetries of its own.

The important observational study by *Corbosiero and Molinari* [2003] showed that the distribution of strong convection is more strongly correlated with vertical shear than with the storm translation vector, although they used lightening frequency as a proxy for inferring the asymmetry of convection. However, the main focus of their study was on moderate to strong shear, and the question remains as to whether storm translation is important in organizing convection in the weak shear case. Although the main purpose of *Frank and Ritchie* [2001] was to investigate the effects of vertical shear in a moist model with an explicit representation of deep moist convection, they did carry out one simulation for a weak uniform flow of 3.5 m s^{-1}. In this they found that ". . . the upward vertical motion pattern varies between periods that are almost axisymmetric and other periods when they show more of a azimuthal wave number-1 asymmetry, with maximum upward motion either ahead or to the left of the track" and "the frictional convergence pattern in the boundary layer causes a preference for convective cells to occur generally ahead of the storm relative to behind it, but this forcing is not strong enough to maintain a constant asymmetric pattern." Although they show only four time snapshots of the cloud water and rainwater fields, the findings are at first sight contrary to all of the predictions of a steady boundary layer forced by an imposed gradient wind field above the boundary layer as in the uniform flow studies cited above. However, the orientation of the rainwater asymmetry is closest to the pattern of vertical motion predicted by *Shapiro* [1983]. Even so, snapshots are insufficient to show whether there is a persistent asymmetric pattern of deep convection in a suitable time average of the evolving flow. Such a time average should span a minimum of several convective life cycles, i.e., at least a few hours.

As noted above, there is disparity in the literature on the orientation of flow asymmetries that arise in the boundary layer, even in the relatively simple configuration with no moist processes. For example, using quasilinear and fully nonlinear, slab boundary layer models with constant depth, *Shapiro* [1983] showed that the strongest convergence (and hence vertical velocity in the slab model) occurs on the forward side of the vortex in the direction of motion (see his Figures 5d and 6c). In contrast, the purely linear theory of *Kepert* [2001, Figure 5, left] predicts that the strongest convergence lies at 45° to the right of the motion and the nonlinear calculations of *Kepert and Wang* [2001, Figure 10, bottom left] predicts it to be at 90° to the right of motion. As acknowledged by *Kepert* and *Kepert* and Wang, a limitation of their studies is the fact that the horizontal flow above the boundary layer is prescribed and not determined as part of a full solution. Moreover, as noted above, there is no guarantee that the ascent predicted by the boundary layer solution can be "ventilated" by the convection and no guarantee that the convection will not modify the prescribed wind structure at the top of the boundary layer.

In addition to the foregoing limitation of the boundary layer models, the presence of deep convection greatly complicates the situation and, as pointed out in M1 and by *Shin and Smith* [2008], the random nature of the inner-core flow asymmetries generated by convection calls for a new methodology to assess differences in the asymmetric flow structure between two particular flow configurations. The reason is that the results of a single deterministic calculation in each configuration may be unrepresentative of a model ensemble in that configuration. Thus one needs to compare the ensemble means of suitably perturbed ensembles of the two configurations, and/or to carry out suitable time averaging (see above). We apply this methodology here to extend the calculations of M1 to the prototype problem for a moving vortex, which considers the evolution of an initially dry, axisymmetric vortex embedded in a uniform zonal flow on a Northern Hemisphere *f*-plane.

The scientific issues raised above motivate three specific questions about the convective organization of a translating vortex:

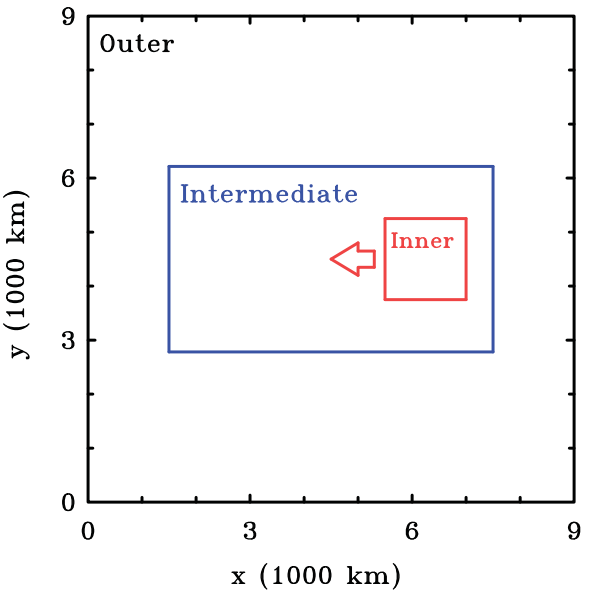

Figure 1. Configuration of the three model domains. The inner domain is moved from east to west (the negative *x* direction) at selected times to keep the vortex core away from the domain boundary.

1. Does the imposition of a uniform flow in a convection-permitting simulation lead to an organization of the inner-core convection to produce persistent azimuthal asymmetries in convergence and vertical motion?
2. If so, how do these asymmetries compare with those predicted by earlier *theoretical studies* where the horizontal flow above the boundary layer is prescribed and moist processes are not considered?
3. How do the asymmetries in low-level flow structure associated with the storm translation compare with those documented in recent *observational studies*?

This paper seeks to answer these questions using a convection-permitting model that is as simple as possible.

The paper is structured as follows. We give a brief description of the model in section 2 and present the results of the control calculations for vortex evolution on an *f*-plane in section 3. In section 4, we describe the ensemble experiments, where, as in M1, the ensembles are generated by adding small moisture perturbations at low levels. We examine the asymmetric structure of boundary layer winds in section 5 and describe briefly a calculation using a different boundary layer scheme in section 6. The conclusions are given in section 7.

2. The Model Configuration

The numerical experiments are similar to those described in M1 and are carried out also using a modified version of the Pennsylvania State University-National Center for Atmospheric Research fifth-generation Mesoscale Model (MM5; version 3.6) [*Dudhia*, 1993; *Grell et al*., 1995]. The model is configured with three domains with sides orientated east-west and north-south (Figure 1). The outer and innermost domains are square, the former 9000 km in size and the latter 1500 km. The innermost domain is moved from east to west at selected times within an intermediate domain with a fixed meridional dimension of 3435 km and a zonal dimension of up to 8850 km, depending on the background wind speed. The first displacement takes place 735 min after the initial time and at multiples of 1440 min (1 day) thereafter. The frequency of the displacement is doubled for a background wind speed of 12.5 m s^{-1}. The distance displaced depends on the background wind speed in the individual experiments. The outer domain has a relatively coarse, 45 km, horizontal grid spacing, reducing to 15 km in the intermediate domain and 5 km in the innermost domain. The two inner domains are two-way nested. In all calculations, there are 24 σ-levels in the vertical, 7 of which are below 850 mb. The model top is at a pressure level of 50 mb. The calculations are performed on an *f*-plane centered at 20°N.

Following Occum's razor principle, we take the view that to obtain an intuitive understanding of the evolution of a translating vortex, it is advantageous to choose the simplest model possible that captures the essence of the physics. In this spirit, we adopt the simple explicit representation of latent heat release in deep convection used in the pioneering studies of Emanuel [see *Bryan and Rotunno*, 2009], one that mimics pseudo-adiabatic ascent. Also, for all but one experiment, we choose the bulk-aerodynamic parameterization scheme for the boundary layer.

In the moisture scheme, if the specific humidity, q, of a grid box is predicted to exceed the saturation specific humidity, $q_s(p,T)$ at the predicted temperature T and pressure p, an amount of latent heat $L(q-q_s)$ is converted to sensible heat raising the temperature by $dT=L(q-q_s)/c_p$. Furthermore, q is set equal to q_s, so that an amount of condensate $dq=q-q_s$ is produced. Here L is the coefficient of latent heat per unit mass

and c_p is the specific heat of dry air at constant pressure. The increase in air parcel temperature increases q_s, so that a little less latent heat than the first estimate needs to be released and a little less water has to be condensed. The precise amount of condensation can be obtained by a simple iterative procedure. Convergence is so rapid that typically no more than four iterations are required.

Kepert [2012] wrote a useful assessment of different boundary layer schemes and recommended against using ones that do not explicitly represent a logarithmic near surface layer, which would include the bulk-aerodynamic parameterization in the MM5 model. However, the existence and physical basis for a traditional logarithmic layer in the innercore of a tropical cyclone has been called into question [*Smith and Montgomery*, 2013]. Furthermore, the model used by Kepert to assess candidate schemes has issues with the boundary conditions at the top of the model. These conditions constrain the flow to return to a *prescribed* gradient wind with zero radial motion, even where the flow is exiting the boundary layer [*Smith et al*., 2015, Appendix C]. To allay concerns regarding the use of the simple bulk scheme, one additional calculation is carried out using the Gayno-Seaman scheme [*Shafran et al*., 2000].

The surface drag and heat and moisture exchange coefficients are modified to incorporate the results of the coupled boundary layer air-sea transfer experiment (CBLAST) [see *Black et al*., 2007; *Zhang et al*., 2009]. The surface exchange coefficients for sensible heat and moisture are set to the same constant, 1.2×10^{-3}, and that for momentum, the drag coefficient, is set to $0.7 \times 10^{-3} + 1.4 \times 10^{-3}(1 - \exp(-0.055|\mathbf{u}|))$, where $|\mathbf{u}|$ is the wind speed at the lowest model level. The fluxes between the individual model layers within the boundary layer are then calculated using a simple downgradient diffusive closure in which the eddy diffusivity depends on strain rate and static stability [*Grell et al*., 1995; *Smith and Thomsen*, 2010].

The exchange coefficient for moisture is set to zero in the two outer domains to suppress the buildup there of ambient Convective Available Potential Energy (CAPE). Because of the dependence of the moisture flux on wind speed, such a buildup would be different in the experiments with different wind speeds. The sea surface temperature is set to a constant 27°C except in one experiment where it was set to 25°C to give a weaker mature vortex. The radiative cooling is implemented by a Newtonian cooling term that relaxes the temperature toward that of the initial profile on a time scale of 1 day. This initial profile is defined in pressure coordinates rather than the model's σ-coordinates so as not to induce a thermal circulation between southern and northern sides of the model domain.

In each experiment, the initial vortex is axisymmetric with a maximum tangential wind speed of 15 m s^{-1} at the surface at a radius of 120 km. The strength of the tangential wind decreases sinusoidally with height, vanishing at the top model level (50 mb). The vortex is initialized to be in thermal wind balance with the wind field using the method described by *Smith* [2006]. The far-field temperature and humidity are based on Jordan's Caribbean sounding [*Jordan*, 1958]. The vortex center is defined as the centroid of relative vorticity at 900 mb over a circular region of 200 km radius from a "first-guess" center, which is determined by the minimum of the total wind speed at 900 mb, and the translation speed introduced later is based on the movement of this center.

2.1. The Control Experiments

Six control experiments are discussed, five with a uniform background easterly wind field, U, and the other with zero background wind. Values of U are 2.5, 5, 7.5, 10, and 12.5 m s^{-1}, adequately spanning the most common range of observed tropical-cyclone translation speeds. All these experiments employ the bulk aerodynamic option for representing the boundary layer and have a sea surface temperature (SST) of 27°C. Two additional experiments have $U = 5$ m s^{-1}, one with an SST of 25°C and the other with the Gayno-Seaman boundary layer scheme.

2.2. Ensemble Experiments

As in M1, sets of ensemble calculations are carried out for each control experiments. These are similar to the control calculations, but have a random perturbation with a magnitude between ± 0.5 g kg^{-1} added to the water-vapor mixing ratio at each of five grid points up to 950 mb at each horizontal location at the initial time. In order to keep the mass field unchanged, the temperature is adjusted at each point to keep the virtual temperature unchanged. A five-member ensemble is constructed for all values of U except $U = 5$ m s^{-1}, for which a 10-member ensemble is used. The 10-member ensemble was the first to be constructed, but subsequent examination of the wind speed maxima for this ensemble suggested that computationally less

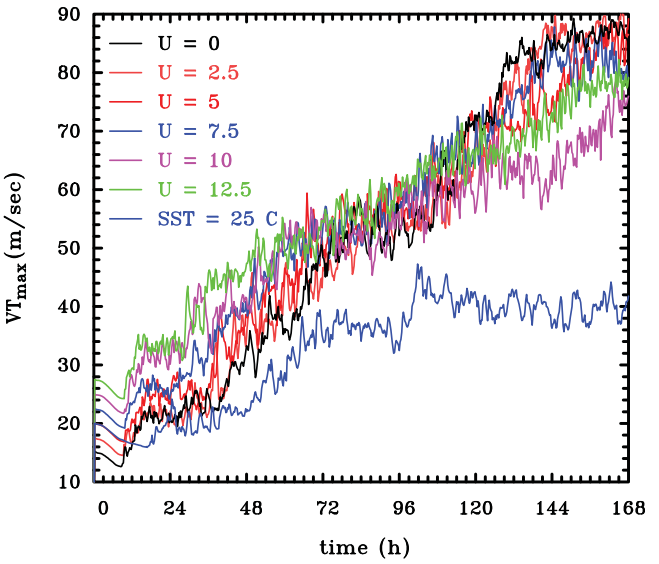

Figure 2. Time series of maximum total wind speed at 850 mb, VT_{max}, for the six experiments with different background wind speeds U in m s^{-1} as indicated, and for the experiment with $U = 5.0$ m s^{-1}, but with the sea surface temperature reduced to 25°C. The time series have been smoothed with a five-point filter to highlight the differences between them.

expensive five-member ensembles would suffice to span the range of variability. On this basis, five-member ensemble plus the control deterministic experiment is used for the other background flow speeds.

3. Results of Five Deterministic Calculations

3.1. Intensity Evolution and Motion

Since the focus of this work is on the asymmetric flow structure, we adopt a metric for intensity based on the maximum *total* wind speed at 850 mb. This metric is perhaps less suitable for theoretical analysis than an azimuthal average of the tangential wind component, but arguably closer to the usage of intensity used by tropical cyclone forecasters. Figure 2 shows time series of the maximum total wind speed, VT_{max} at 850 mb (approximately 1.5 km high) during a 7 day (168 h) integration in the six control experiments and in that with $U = 5$ m s^{-1} and an SST of 25°C. The last experiment will be discussed in section 3.3. As in many previous experiments, the evolution begins with a gestation period during which the vortex slowly decays due to surface friction, but moistens in the boundary layer due to evaporation from the underlying sea surface. This period lasts approximately 9 h during which time the maximum total wind speed decreases by about 2 m s^{-1}.

The imposition of friction from the initial instant leads to inflow in the boundary layer and outflow above it, the outflow accounting for the initial decrease in tangential wind speed through the conservation of absolute angular momentum. The inflow is moist and as it rises out of the boundary layer and cools, condensation progressively occurs in some grid columns interior to the corresponding radius of maximum tangential wind speed. In these columns, existing cyclonic relative vorticity is stretched and amplified leading to the formation of localized deep vortical updraughts. Collectively, these updraughts lead to the convergence of absolute angular momentum above the boundary layer and thereby to the spin-up of the bulk vortex [see e.g., *Bui et al*., 2009]. Then, as the bulk vortex intensifies, the most intense tangential wind speeds develop in the boundary layer [*Smith et al*., 2009].

As the updraughts develop, there ensues a period lasting about 5 days during which the vortex progressively intensifies. During this time, VT_{max} increases from its minimum value of between 12.5 and 25 m s^{-1} to a final value of up to 90 m s^{-1} at the end of the experiment. The vortex in the quiescent environment is the first to attain a mature state after about 6 days, but all except possibly that for $U = 10$ m s^{-1} appear to have reached such a state by 7 days. For all values of U, there are large fluctuations in VT_{max} (up to ± 5 m s^{-1} before time-smoothing) during the period of intensification. Indeed, except in the experiment with an SST of 25°C, the fluctuations in an individual experiment during this period are comparable with the maximum deviations between the different experiments to the extent that it is pertinent to ask if the differences between these experiments are significant. We examine this question in section 4.

The translation speed (calculated as detailed in section 2) tends to be fractionally smaller than the background wind speed, especially in the mature stage when it is between 20% and 25% less. The translation speeds for U=7.5, 10, and 12.5 m s^{-1} are about 5.9, 7.5, and 9.5 m s^{-1}, respectively. The reason for the lower translation speed is presumably the effect of friction, because it can be shown analytically that an upright baroclinic vortex with arbitrary vertical and radial structure in a uniform flow on an *f*-plane is simply advected by this flow.

3.2. Structure Changes

To provide a flavor for the evolution in vortex structure during the intensification period, we show in Figures 3 and 4 contours of vertical velocity at 850 mb at selected times for the control experiment with a westward translation speed of $U = 5$ m s^{-1}. At early times, convective cells begin to develop in the forward left (i.e., southwest) quadrant (Figure 3a), where, as shown below, the boundary-layer-induced convergence is large. However, cells subsequently develop clockwise (upstream in the tangential circulation) in the space of 2 h to the forward quadrant (Figure 3b) and over the next 2 h to the forward-right and rear-right quadrants (Figure 3c). The increased surface moisture fluxes (not shown) on the right side of the storm, where the earth-relative wind speeds are stronger, may play a role in supporting convection also. It should be emphasized that, as in the calculations in M1, the convective cells are deep, extending into the upper troposphere (not shown here).

By 24 h, convective cells are distributed over all four quadrants with little obvious preference for a particular sector. However, as argued earlier, because of the stochastic nature of convection, one cannot make a general statement about flow asymmetries from a snapshot of the flow at a particular time. Note also that the convective cells at this time are rotating cyclonically around the vortex. The convective cells amplify the vertical component of local low-level relative vorticity by one or 2 orders of magnitude (not shown). For comparison, Figures 3e and 3f show the early evolution of cells in the control calculation with zero background flow, which, as expected, displays no preference for cells to develop in a particular sector.

As time proceeds, the convection becomes more organized (Figure 4), showing distinctive banded structures, but even at 96 h, its distribution is far from axisymmetric, even in the region within 100 km of the axis. However, as shown later (see Figure 8), the vortex does develop an annular ring of convection with an eye-like feature toward the end of the integration.

Figure 5 shows the pattern of divergence at a height of 500 m averaged between 3 and 5 h and 6.75 to 7 days in the case with $U = 5$ m s^{-1}. The 6 h averaging period is chosen to span a reasonable number of fluctuations in the azimuthally averaged tangential wind field shown in Figure 2 before the curves are smoothed. However, the pattern of divergence is not appreciably different when a 12 h period is chosen. The height 500 m is typically that of the maximum tangential wind speed and about half that of the "mean" inflow layer in the mature stage (see section 5). The period 3–5 h is characteristic of the gestation period during which the boundary layer is moistening, but before convection has commenced. During this period, the convergence is largest on the forward side of the vortex, explaining why the convective instability is first released on this side. There is a region of divergence in the rear left sector. The pattern is similar to that predicted by *Shapiro* [1983, Figure 5d, but note that the vortex translation direction is oriented differently to that in our configuration]. In Shapiro's calculation, which, at this stage was for a stronger symmetric vortex with a maximum tangential wind speed of 40 m s^{-1} translating at a speed of 10 m s^{-1}, the divergence region extends also to the rear right of the track.

In the mature stage in our calculation, the pattern of divergence is rather different from that in Shapiro's calculation and is much more symmetric, presumably because at this stage the vortex is twice as strong as Shapiro's and the translation speed is only half. Notably, outside the ring of strong convergence that marks the eyewall, the vortex is almost surrounded by a region of low-level divergence, except for the narrow band of convergence wrapping into the eyewall from the forward right to the forward left quadrants. In the next section we examine the differences in behavior for a weaker vortex.

It is perhaps worth remarking that the ring of divergence inside the ring of strongest convergence in Figure 5c is associated with the upflow from the boundary layer, which is being centrifuged outward as part of the adjustment of this supergradient flow to a state of local gradient wind balance [*Smith et al*., 2009]. The area of convergence in the small central region of the vortex is presumably the weak Ekman-like pumping one would expect in a rotating vortex with weak frictional inflow in the boundary layer.

3.3. Calculations for a Weaker Vortex

To examine the questions raised in the previous section concerning possible differences when the vortex is much weaker, we repeated the experiment with $U = 5$ m s^{-1} with the sea surface temperature reduced by 2°C to 25°C. Figure 2 shows the variation of total wind speed at 850 mb in this case. The maximum wind speed during the mature stage is considerably reduced compared with that in the other experiments, with the average wind speed during the last 6 h of the calculation being only about 40 m s^{-1}. However, as

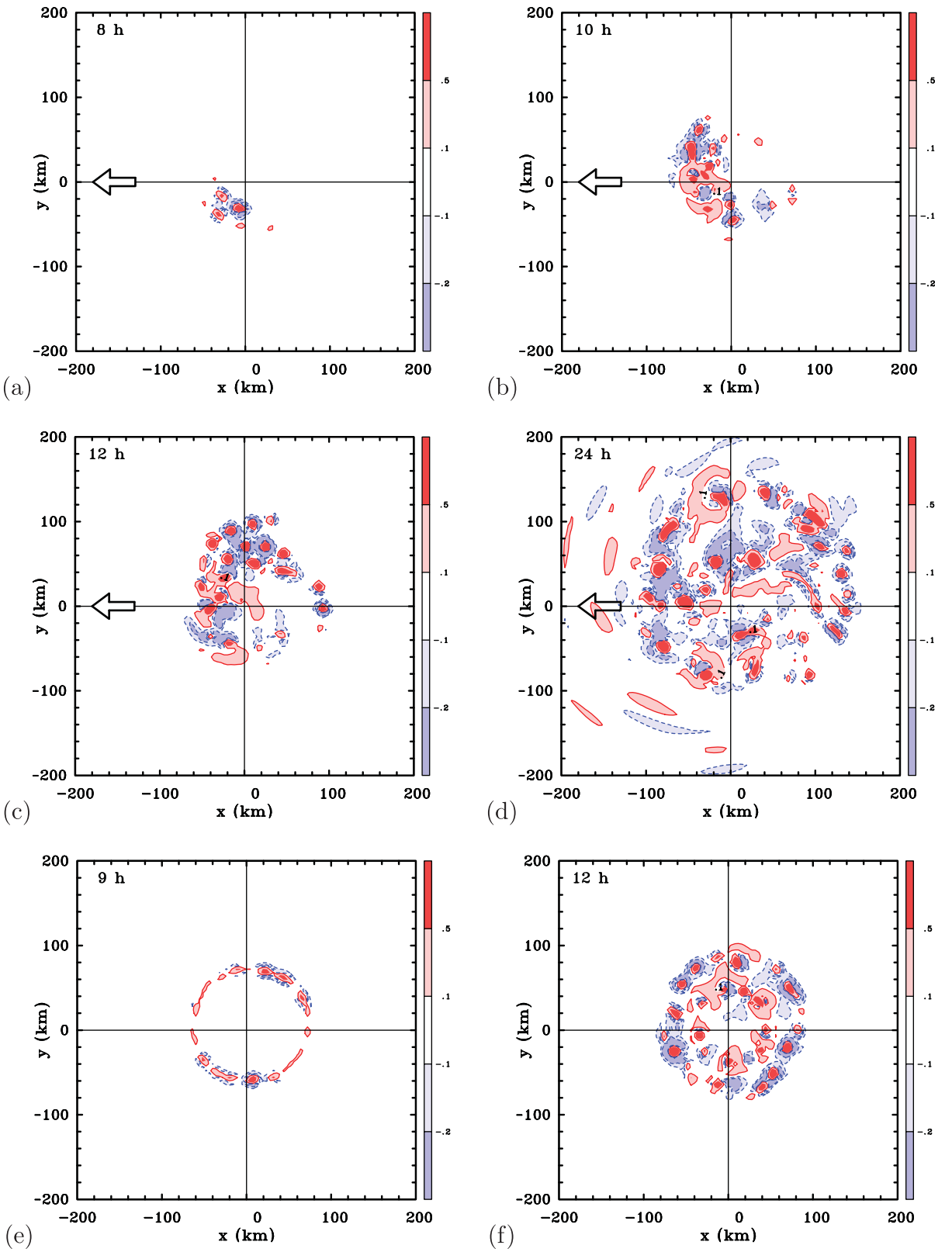

Figure 3. Patterns of vertical velocity at 850 mb at times indicated in the top left of each figure during the vortex evolution. (a–d) For the experiment with $U = 5$ m s^{-1} (from left to right), and (e and f) for the experiment with the zero background flow. Contour levels as indicated by label bar in m s^{-1}. Positive velocities: solid contours, light red, and red shading; negative velocities: dashed lines, light blue, and blue shading. The zero contour is not plotted. The arrow indicates the direction of vortex motion where applicable.

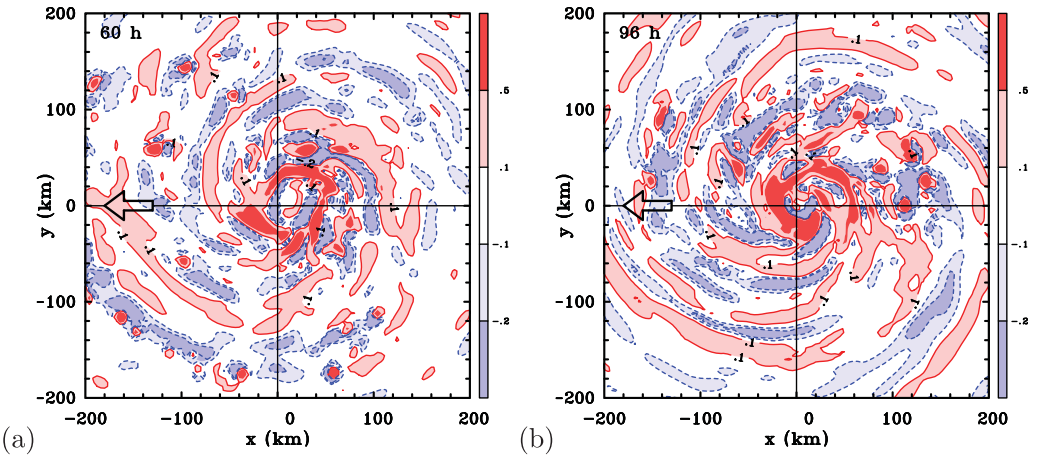

Figure 4. Patterns of vertical velocity at 850 mb at (a) 60 h and (b) 96 h, during the vortex evolution for the experiment with $U = 5.0$ m s^{-1}. Contour levels as indicated by color bar in m s^{-1}. Positive velocities: solid contours, light red, and red shading; negative velocities: dashed lines, light blue, and blue shading. The zero contour is not plotted. The arrow indicates the direction of vortex motion where applicable.

expected, the evolution in vertical velocity at 850 mb is similar to that in Figure 3. Figure 6 shows the patterns of divergence at a height of 500 m averaged during 3–5 h and during the last 6 h of this calculation. These should be compared with the corresponding fields in Figure 5. In the early period (Figure 5a), the patterns are much the same, although the maximum magnitudes of asymmetric divergence and convergence are slightly larger when the sea surface temperature is reduced. A plausible explanation for this difference is the reduced Rossby elasticity in the weaker vortex [*McIntyre*, 1993]. In the mature stage (Figure 5b), the central ring of divergence marking the eye is much larger in the case of the weaker vortex and the region of convergence surrounding it that marks the eyewall is broader and more asymmetric. Like the stronger vortex and that in Shapiro's calculation, the largest convergence remains on the forward side of the vortex with respect to its motion. Of course, the motion-induced asymmetry in the convergence field is much more pronounced in the case of the weaker vortex.

4. Ensemble Experiments

As pointed out by M1 and *Shin and Smith* [2008], the prominence of deep convection during the vortex evolution and the stochastic nature of convection, itself, means that the vortex asymmetries will have a

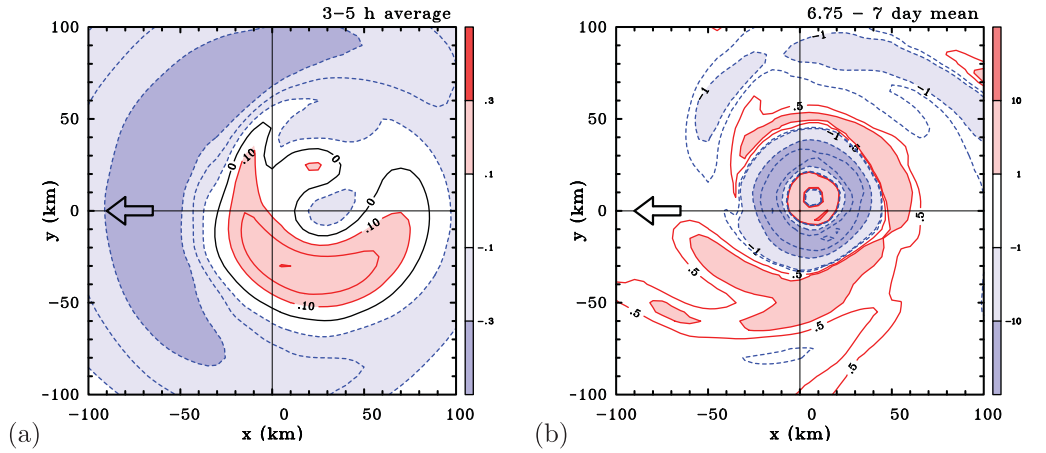

Figure 5. Patterns of divergence at 500 m for the experiment with $U = 5$ m s^{-1}. (a) Averaged every 15 min between 3 and 5 h (contour interval 1×10^{-5} s^{-1}). Positive contours (solid/red) and negative values (dashed/blue), thin zero contour black, shading levels, and colors indicated on the label bar ($\times10^{-4}$). (b) Averaged every 15 min between 6.75 and 7 days (contour interval: thick contours 1×10^{-3} s^{-1}, thin contours 5×10^{-5} s^{-1} and 1×10^{-4} s^{-1}. Positive contours (solid/red), negative values (dashed/blue)), zero contour not shown, shading levels and colors indicated on the label bar ($\times10^{-4}$). The arrow indicates the direction of vortex motion. Note that the domain shown is only half the size of that in Figures 3 and 4.

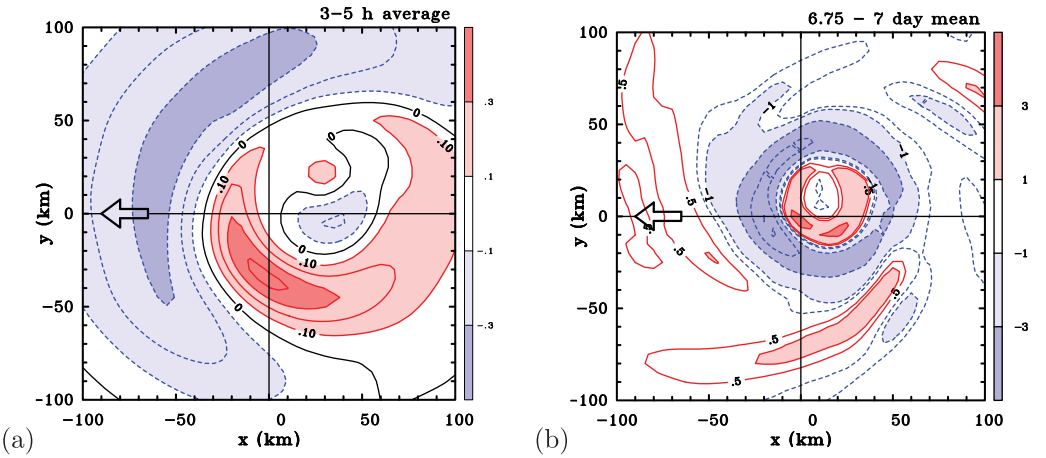

Figure 6. Patterns of divergence at 500 m for the experiment with $U = 5$ m s^{-1} and a sea surface temperature of 25°C: (a) Averaged every 15 min between 3 and 5 h and (b) between 6.75 and 7 days. Contour levels and shading as in the corresponding plots of Figure 5. The arrow indicates the direction of vortex motion. Note that the domain shown is only half the size of that in Figure 4.

stochastic component also. Thus, a particular asymmetric feature brought about by an asymmetry in the broad-scale flow (in our case the uniform flow coupled with surface friction) may be regarded as significant only if it survives in an ensemble of experiments in which the details of the convection are different. For this reason, we carried out a series of ensemble experiments in which a random moisture perturbation is added to the initial condition in the control experiments as described in section 2.2. We begin by investigating the effects of this stochastic component on the vortex intensification and go on to examine the effects on the vortex structure in the presence of uniform flows with different magnitudes.

4.1. Stochastic Nature of Vortex Evolution

For simplicity, we examine first the time series of the ensemble mean of the maximum total wind speed, VT_{max}, at 850 mb for two of the control experiments, those with background flows of 5 and 10 m s^{-1}. These are shown in Figure 7a, together with the maximum and minimum values of VT_{max} at each time. The latter indicate the range of variability for each set of ensembles. There are two features of special interest:

1. Although the ensemble mean intensity of the run with $U = 5$ m s^{-1} is lower than that with $U = 10$ m s^{-1} at early times, with little overlap of the ensemble spread, the mean with $U = 5$ m s^{-1} exceeds that of $U = 10$ m s^{-1} after about 108 h, even though there remains a region of overlap in the ensemble spread to 168 h.
2. There is a notable difference between the maximum and minimum intensity in a particular ensemble set at any one time, being as high as 20 m s^{-1} in the case $U = 10$ m s^{-1} at about 6 days.

The foregoing comparison provides a framework for reexamining the differences in intensity between the control experiments with different values of background flow shown in Figure 2. The comparison affirms the need to examine ensemble-mean time series rather than those of single deterministic runs. A comparison corresponding with the deterministic runs of Figure 2 is made in Figure 7b, which shows time series of the ensemble mean for the experiments with $U = 0$, 5, 7.5, 10, and 12.5 m s^{-1}. It is clear from this figure that the intensification rate decreases broadly with increasing background flow speed and that the mature vortex intensity decreases also, although there is a period of time, between about 96 and 168 h (4 and 7 days) when the ensemble-mean intensity for $U = 10$ is less than that for $U = 12.5$ m s^{-1}. Moreover, the differences between the intensity of the pairs of ensembles with $U = 5$ and 7.5 m s^{-1} and $U = 10$ and 12.5 m s^{-1} at 7 days are barely significant. Finally we note that comparison of plots of the eleven (including the control calculation as part of the ensemble mean when averaging) VT_{max}-time series for $U = 5$ m s^{-1} with the six such time series for the other ensemble sets suggests that five ensembles together with the corresponding control experiment give an acceptable span of the range of variability in intensity in each case (not shown).

A question is whether the above results are consistent with observations. A pertinent study in this regard is that of *Zeng et al.* [2007], who presented observational analyses of the environmental influences on storm intensity and intensification rate based on reanalysis and best track data of northwest Pacific storms. While

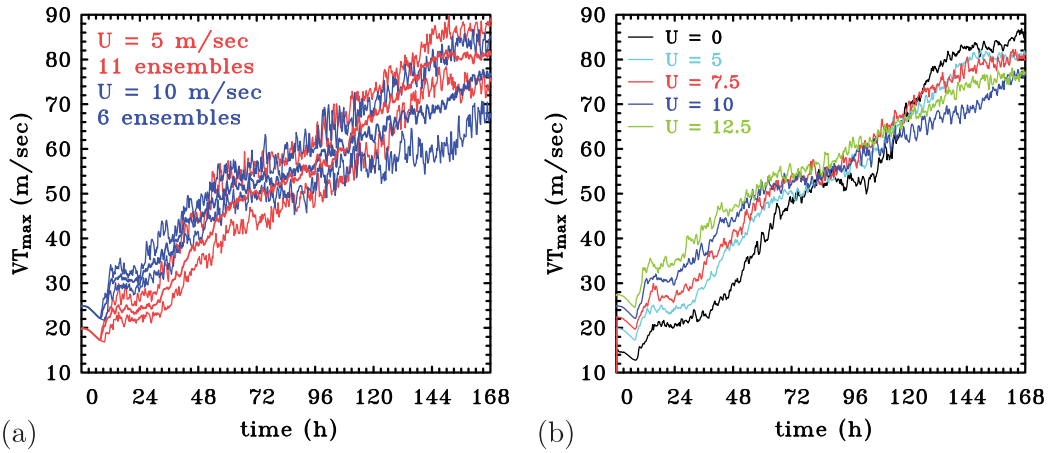

Figure 7. (a) Time series of the ensemble-mean, maximum total wind speed, VT_{max}, at 850 mb for the control experiments with a background flow of 5 m s^{-1} (middle red curve) and 10 m s^{-1} (middle blue curves). The thin curves of the same color show the maximum and minimum values of VT_{max} for a particular run at a given time. (b) Time series of the ensemble-mean VT_{max} for the experiments with U=0, 5, 7.5, 10, and 12.5 m s^{-1}.

they considered a broader range of latitudes, up to 50°N, and of storm translation speeds of up to 30 m s^{-1}, the data that are most relevant to this study pertain to translation speeds between 3 and 12 m s^{-1}. They found that the most intense tropical cyclones (their Figure 3a) and those with the most rapid intensification rates [*Zeng et al.*, 2007, Figure 6a] occur in this speed range when there is relatively weak vertical shear. In particular, they found that "generally the intensification rate ... increases with decreasing translation speed ..." However, their data do not show a clear one-to-one relationship between intensity and translation speed.

An investigation of the precise reasons why a uniform flow reduces the rate of intensification and mature intensity as the background flow increases is beyond the scope of this study and would require a paper in its own right.

4.2. Stochastic Nature of Vortex Structure

Figures 8a–8d show the time-averaged vertical velocity fields for the last 6 h of integration (6.75 to 7 days) in three of the experiments with $U = 10$ m s^{-1}, including the control experiment and two ensemble experiments from the six-member ensemble mean. In all fields, including the ensemble mean, there is a prominent azimuthal wave number-1 asymmetry, with maximum upflow in the forward left quadrant and maximum subsidence in the eye to the left of the motion vector. Similar results are obtained for $U = 7.5$ and 12.5 m s^{-1} (not shown). Inspection of the field for $U = 5$ m s^{-1} suggests that the most prominent asymmetry in the upward vertical velocity is at azimuthal wave number-4 (Figure 8f), which is a feature also of the ensemble mean of calculations for a quiescent environment (Figure 8e). Since the case of a quiescent environment would be expected to have no persistent asymmetry for a sufficiently large ensemble, we are inclined to conclude that the wave number-4 asymmetry in the case with $U = 5$ m s^{-1} is largely a feature of the limited grid resolution (the 100 km square domain in Figure 8 is spanned by only 21 × 21 grid points). Therefore, we would be cautious of attributing much significance to the wave number-4 component of the asymmetry in Figures 8e and 8f.

On the basis of these results, we are now in a position to answer the first of the three questions posed in the Introduction: does the imposition of a uniform flow in a convection-permitting simulation lead to an organization of the innercore convection so as to produce asymmetries in low-level convergence and vertical motion? The answer to this question is a qualified yes, the qualification being that the effect is barely detectable for the (mostly) strong vortices that arise in our calculations for background flow speeds below about 7 m s^{-1}. However, the effect increases with background flow speed and there is a prominent azimuthal wave number-1 asymmetry in the calculation for a weaker storm with $U = 5$ m s^{-1} (see section 3.3 and Figure 6b).

We are in a position also to answer the second of the three questions: how do the asymmetries compare with those predicted by earlier studies? For background flow speeds of 7.5 m s^{-1} and above, the ensemble mean vertical velocity asymmetry, which has a maximum velocity in the forward left quadrant in our

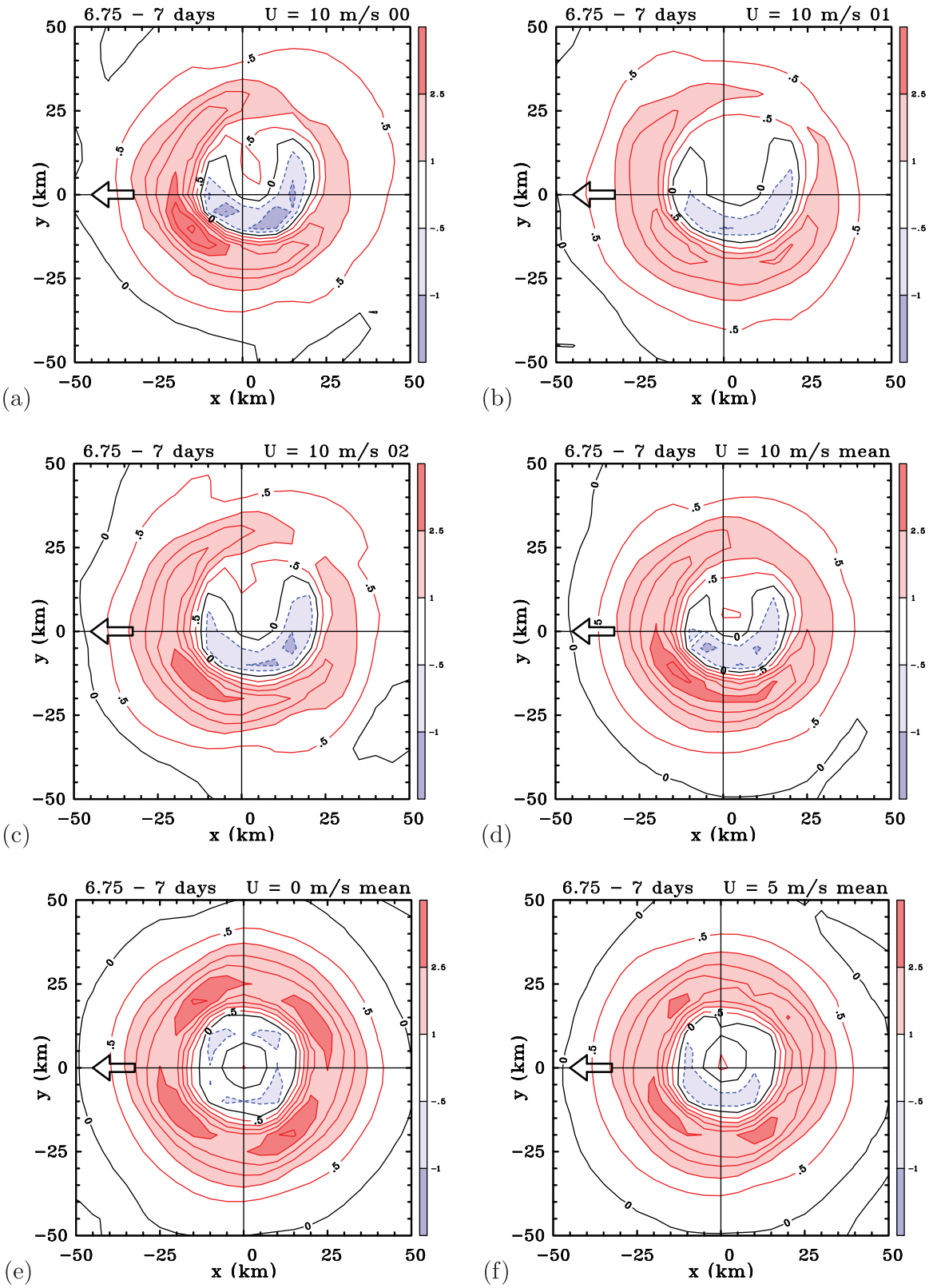

Figure 8. Patterns of vertical velocity at 850 mb averaged every 15 min during the period 6.75 and 7 days about the center of minimum total wind speed at this level. (a–d) The experiments with $U = 10$ m s^{-1}; (a) the control experiment; (b and c) two ensemble experiments; and (d) the average of the control and five ensemble experiments. For comparison, Figures 8e and 8f show the ensemble mean fields for the experiments with $U = 0$ m s^{-1} and $U = 5$ m s^{-1}, respectively. Contour interval: 0.5 m s^{-1}. Shading levels as indicated by label bar in m s^{-1}. Positive velocities (solid contours, pink, and red shading), negative velocities (dashed lines, light, and dark blue shading), and zero contour (thin, solid, and black). The arrow indicates the direction of vortex motion.

calculations, is closest to the predictions of *Shapiro* [1983]. These predictions are based on solutions of a truncated azimuthal spectral model for the boundary layer of a translating vortex. In his nonlinear solution, Shapiro found the maximum convergence (and hence vertical motion in his slab model) to be in the direction of storm motion, while we find it to be approximately 45° to the left thereof. A likely explanation for this difference is that in Shapiro's calculation, the maximum in the total wind asymmetry above the boundary layer is to the right of the motion vector, whereas in our case it is about 45° to the right. This difference arises because, in our calculations, the vortex flow just above the boundary layer is determined as part of a full solution for the flow and is not prescribed. In other words, if the asymmetric pattern of vertical motion at the top of the boundary layer predicted by Shapiro's theory does lead to an earth-relative asymmetry in the envelope of convection, the asymmetric flow induced by this envelope will modify the distribution of horizontal flow and pressure at the top of the boundary layer, thereby altering the structure of ascent induced by the boundary layer at its top and so on.

Shapiro analyzed also linear and "quasi-linear" truncations. He noted that the solution of the linear truncation is inaccurate in characterizing the asymmetries. In the quasi-linear truncation, the feedback from wave number-1 and wave number-2 to wave number-0 and wave number-1 in the nonlinear advective terms is neglected (i.e., backscatter is neglected). While there are some small quantitative differences between the quasi-linear and nonlinear solutions, the patterns of the flow asymmetries are similar (compare his Figures 5 and 6). Based on his analyses, Shapiro offers a clear articulation and quantification of the self-sharpening effect of azimuthal wave scattering on the translating mean vortex. We conclude that Shapiro's nonlinear model provides an acceptable zero-order description of the boundary layer asymmetries that survive the transient effects of deep convection, especially when taking into account the different orientations of the maximum total wind asymmetry discussed above.

The asymmetry in vertical velocity in our model deviates significantly from that in *Kepert*'s [2001] linear theory, where the maximum vertical velocity is at 45° to the *right* of the motion vector (see his Figure 5, left) and even more from that in the nonlinear numerical calculation of *Kepert and Wang* [2001], where the maximum is at 90° to the *right* of the motion vector (see their Figure 10). The reasons for the discrepancies between Shapiro's results and those of *Kepert* [2001] and *Kepert and Wang* [2001] are unclear: although the last two papers cited Shapiro's earlier work, surprisingly they did not comment on the differences between their findings and his. In a very recent study of the steady symmetric and asymmetric boundary layer response of a translating tropical cyclone vortex, *Williams* [2015, p. 17] presents results that appear to support Shapiro's prediction of the asymmetric pattern of vertical motion. However, it is difficult to discern the evidence for this support based on the figure referred to, namely Figure 13b. In the text, it is stated that this figure shows the asymmetric component of the flow in the slab boundary case, but actually it shows vertical profiles of terms in the steady state absolute angular momentum equation, presumably from the multilevel model!

4.3. Wind Asymmetries

Figure 9 show contours of *total wind speed* in the Earth-relative frame at 850 mb averaged during the period 6.75 to 7 days for the control experiment with $U = 10$ m s^{-1}, two ensembles for this value and the ensemble mean (control + five ensembles). In constructing the time average, the vortex at each time is centered on the center of minimum total wind speed at this time and level. To help interpret the patterns shown, we recall that in the simple case of an axisymmetric vortex translating in a uniform flow, there is an azimuthal wave number-1 asymmetry in the Earth-relative frame. In this case, the strongest earth-relative winds lie to the right of the track where the ambient winds reinforce those due to the vortex [see e.g., *Callaghan and Smith*, 1998]. (In the Southern Hemisphere, the strongest winds lie to the left of the track.) Our calculations for a moist frictional vortex show that the asymmetry in total wind speed above the boundary layer is shifted to the forward right sector. At present, we know of no existing theory to explain this shift for the flow above the boundary layer. Note that the maximum wind speed is weaker in ensemble 1 (Figure 9b) than in ensemble 2 (Figure 9c) and largest in the control experiment (Figure 9a). Significantly, the maximum in the forward right quadrant survives in the ensemble mean, again an indication that this maximum is a robust asymmetric feature.

5. Asymmetry of Boundary Layer Winds

We seek now to answer the third question posed in section 1, i.e., how do the asymmetries in low-level flow structure associated with the storm translation compare with those documented in recent *observational*

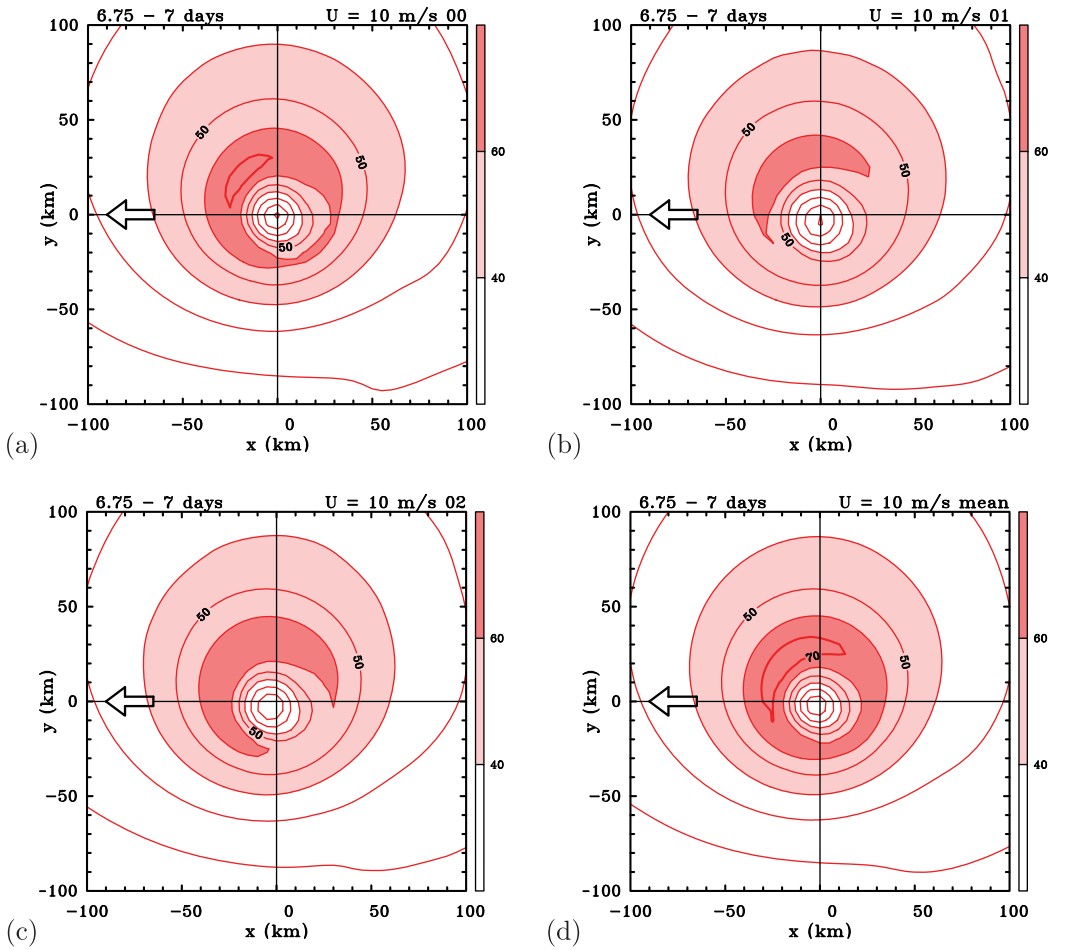

Figure 9. Patterns of total wind speed at 850 mb in an Earth-relative frame (a–d) averaged every 15 min during the period 6.75 and 7 days about the center of minimum total wind speed at this level. (a) The control experiment and (b and c) two ensemble experiments with $U = 5$ m s^{-1}. Figure 9d shows the average of the control and 10 ensemble experiments. Contour interval: thin contours 10 m s^{-1}. Values between 40 and 60 m s^{-1} shaded light red, values exceeding 60 m s^{-1} shaded red. The arrow indicates the direction of vortex motion.

studies? In a series of papers, *Kepert* [2006a, 2006b] and *Schwendike and Kepert* [2008] carried out a detailed analysis of the boundary layer structure of four hurricanes based on Global Positioning System dropwindsonde measurements, complementing the earlier observational study of *Powell* [1982]. Among the effects noted by *Kepert* [2006a] for Hurricane Georges (1998) were that the low-level maximum of the tangential wind component "becomes closer to the storm center and is significantly stronger (relative to the flow above the boundary layer) on the left of the storm than the right." He noted also that "there is a tendency for the boundary layer inflow to become deeper and stronger toward the front of the storm, together with the formation of an outflow layer above, which persists around the left and rear of the storm." We examine now whether such features are apparent in the present calculations.

Figure 10 shows height-radius cross sections of the tangential and radial wind component in the comoving frame in different compass directions for the control calculation with a prescribed zonal wind speed of $U = 5$ m s^{-1}. Figures 10a and 10b show time-averaged isotachs of the tangential winds in the last 6 h of the calculation in the west-east (W-E) and south-north (S-N) cross sections to a height of 3 km. These do show a slight tendency for the maximum tangential wind component at a given radius to become lower with decreasing radius as the radius of the maximum tangential wind is approached. Moreover, the maximum tangential wind speed occurs on the left (i.e., southern) side of the storm as found by Kepert. In fact, the highest wind speeds extend across the sector from southwest to southeast and the lowest winds in the sector northeast to northwest. (The maximum tangential wind speeds in the various compass directions are: W 77.1 m s^{-1}, SW 85.9 m s^{-1}, S 85.9 m s^{-1}, SE 84.0 m s^{-1}, E 78.3 m s^{-1}, NE 73.7 m s^{-1}, N 71.0 m s^{-1}, and NW 73.9 m s^{-1}).

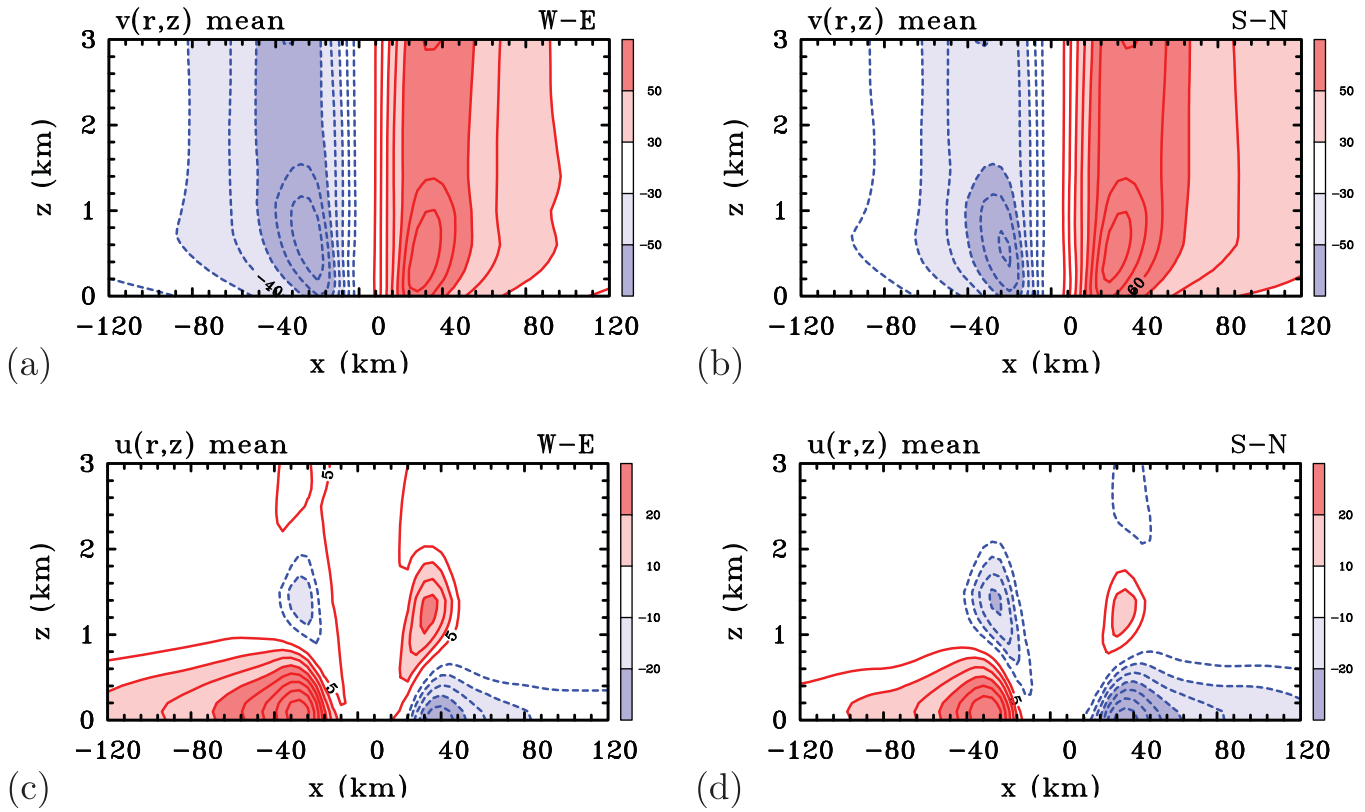

Figure 10. Height-radius cross sections showing the isotachs of the tangential and radial wind components in the main compass directions (x) in the comoving frame. The data are for the control calculation with $U = 5$ m s^{-1} and are averaged every 15 min during the period 6.75 and 7 days. Tangential component: (a) west to east, (b) south to north. Radial component: (c) west to east, (d) south to north. Contour values: 10 m s^{-1} for tangential wind, 5 m s^{-1} for the radial wind. Positive contours (tangential wind component into the page, radial wind component in the x direction) are denoted by solid/red and negative contours are denoted by dashed/blue. The zero contour is not plotted. Shading levels as indicated on the label bar.

Figures 10c–10f show the corresponding time-averaged isotachs of the radial winds in the west-east, southwest-northeast (SW-NE), south-north, and southeast-northwest (SE-NW) cross sections. The strongest and deepest inflow occurs in the sector from northwest to southwest (i.e., the sector centered on the direction of storm motion) and the weakest and shallowest inflow in the sector southeast to east. (The maximum radial wind speeds in the various compass directions are: W 43.5 m s^{-1}, SW 39.3 m s^{-1}, S 34.8 m s^{-1}, SE 29.7 m s^{-1}, E 29.1 m s^{-1}, NE 33.1 m s^{-1}, N 38.5 m s^{-1}, and NW 42.6 m s^{-1}). These results are broadly consistent with the Kepert's findings. Note that, in contrast to Shapiro's study, there is inflow in all sectors, presumably because of the much stronger vortex here.

The strongest outflow lies in the south to southeast sector (Figures 10c and 10d), which is broadly consistent also with Kepert's findings for Hurricane Georges.

While the azimuthally averaged radial velocity component may appear to be somewhat large in some of the cross sections, we would argue that the values are not unreasonable. For example, *Kepert* [2006a, Figure 9] shows mean profiles with inflow velocities on the order of 30 m s^{-1} for Hurricane Georges (1998) with a mean near-surface tangential wind speed of over 60 m s^{-1}. Moreover, *Kepert* [2006b, Figure 6] shows maximum inflow velocities for Hurricane Mitch (1998) on the order of 30 m s^{-1} with a mean near-surface tangential wind speed on the order of 50 m s^{-1}. In our calculations the mean total near-surface wind speed is on the order of 75 m s^{-1}. The boundary layer composite derived from dropsondes released from research aircraft in Hurricane Isabel (2003) in the eyewall region by *Montgomery et al.* [2006] shows a similar ratio of 0.5 between the maximum mean near-surface inflow to maximum near-surface swirling velocity. The recent dropsonde composite analysis of many Atlantic hurricanes by *Zhang et al.* [2011a] confirms that a ratio of 0.5 for the mean inflow to mean swirl for major hurricanes is typical near the surface.

At this time, there does not appear to be a satisfactory theory to underpin the foregoing findings concerning the asymmetry in the depth of the inflow, which is an approximate measure for the boundary layer

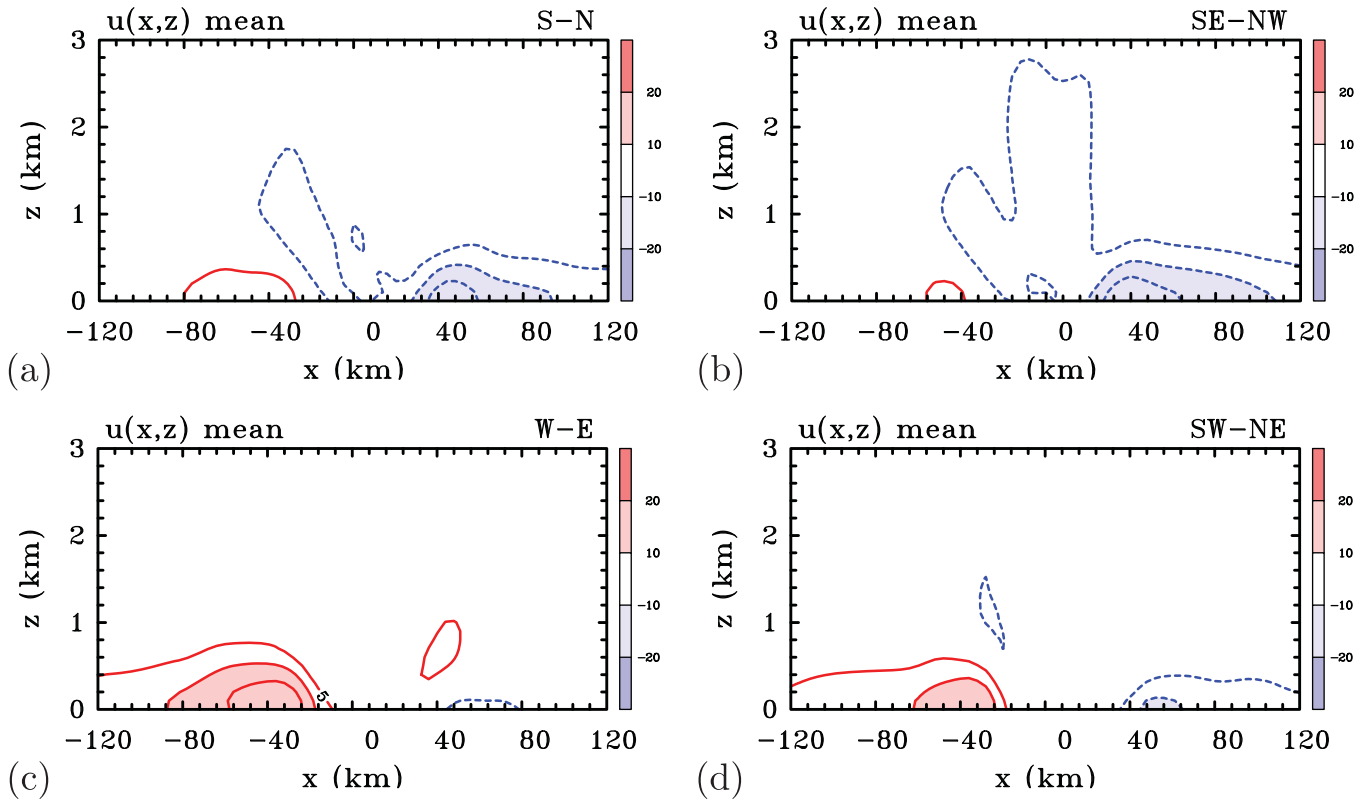

Figure 11. Height-radius cross sections showing isotachs of the wind component in different compass directions (x) in the comoving frame. The data are for the control calculation with $U = 5$ m s^{-1} and a sea surface temperature of 25°C, and are averaged every 15 min during the period 6.75 and 7 days. (a) South to north, (b) southeast to northwest, (c) west to east, (d) southwest to northeast. Contour values: 5 m s^{-1}. Positive contours solid/red, negative contours dashed/blue. The zero contour is not plotted. Shading levels as indicated on the label bar.

depth. Of the two theories that we are aware of, *Shapiro*'s [1983] study assumes a boundary layer of constant depth, but it does take into account an approximation to the nonlinear acceleration terms in the inner core of the vortex. In contrast, *Kepert* [2001] presents a strictly linear theory that accounts for the variation of the wind with height through the boundary layer and the variation of boundary layer depth with azimuth, but the formulation invokes approximations whose validity are not entirely clear to us. For example, he assumes that the background steering flow is in geostrophic balance, but notes that "the asymmetric parts of the solution do not reduce to the Ekman limit for straight flow far from the vortex." In addition, he assumes that the tangential wind speed is large compared with the background flow speed, an assumption that is not valid at large radii where the tangential wind speed of the vortex becomes small. Further, in the inner-core region, linear theory is not formally valid for both the symmetric flow component [*Vogl and Smith*, 2009] and asymmetric flow component [*Shapiro*, 1983, Tables 1 and 2]. Thus, it is difficult for us to precisely identify a region in radius where the theory might be applicable.

In fluid-dynamical terms one might argue that, as the boundary layer wind speeds increase, the boundary layer depth decreases since the local Reynolds number increases. However, such an argument does not explain the depth behavior seen in Figure 10 unless the vertical eddy diffusivity increases appreciably with decreasing radius. The results of *Braun and Tao* [2000, Figure 15] and *Smith and Thomsen* [2010, Figure 8] show that such an increase could occur.

In the case of a weaker vortex (Figure 11), the strongest inflow occurs also in the sector from west through northwest to north (the forward right sector relative to the motion), but the magnitude of the radial inflow is weaker than in the case of the stronger vortex (compare Figures 11a–11d with Figures 10c–10f, respectively). In contrast, the inflow in the sector from south through southeast to east (the rear left sector relative to the motion) is weak.

We have examined recent observational papers of possible relevance to our study including *Zhang and Ulhorn* [2012], *Rogers et al.* [2012], and *Zhang et al.* [2013]. The first of these papers gives statistics of surface inflow

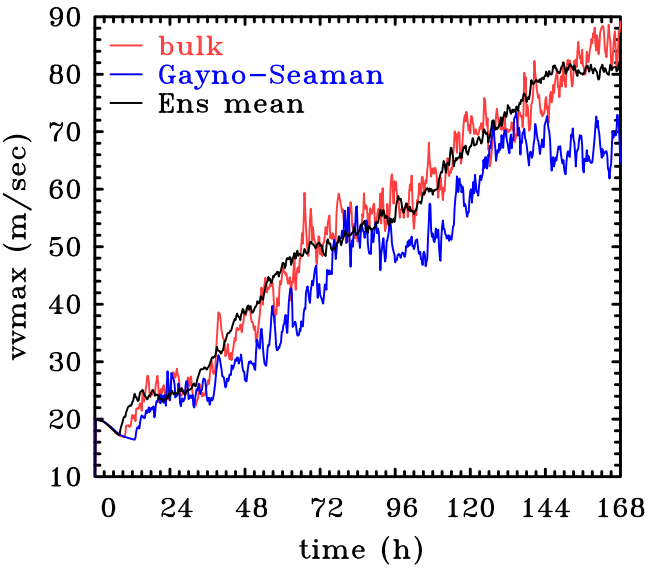

Figure 12. Time series of maximum total wind speed at 850 mb for the control experiments with $U = 5$ m s^{-1} (bulk/red curve), the corresponding ensemble mean (Ens mean/black curve), and the experiment using the Gayno-Seaman boundary layer scheme (blue curve).

angles only for composite storms and these data have large scatter. For these reasons, this study seems only marginally relevant to ours. Rogers et al. is a composite study of axisymmetric storm structure based on Doppler radar analyses and dropsonde data and, because of its focus on the axisymmetric structures, is not directly applicable also. Finally, *Zhang et al.* [2013] examine the boundary layer asymmetries associated with deep vertical shear, but interestingly they did write on p3980: "As the boundary layer dynamics in a rotating system are closely related to storm motion [*Shapiro*, 1983; *Kepert and Wang*, 2001], our future work will investigate the asymmetric boundary layer structure relative to the storm motion as well." We think the current work will lay useful groundwork for such a study.

6. The Gayno-Seaman Boundary Layer Scheme

The foregoing calculations are based on one of the simplest representations of the boundary layer. It is therefore pertinent to ask how the results might change if a more sophisticated scheme were used. A comparison of different schemes in the case of a quiescent environment was carried out by *Smith and Thomsen* [2010], where it was found that the bulk scheme used here is one of the least diffusive. For this reason, we repeated the control calculation with $U = 5$ m s^{-1} with the bulk scheme replaced by the Gayno-Seaman scheme. The latter is one of the more diffusive schemes examined by *Smith and Thomsen* [2010], giving a maximum eddy diffusivity, K, of about 250 m^2 s^{-1}. This value is considerably larger

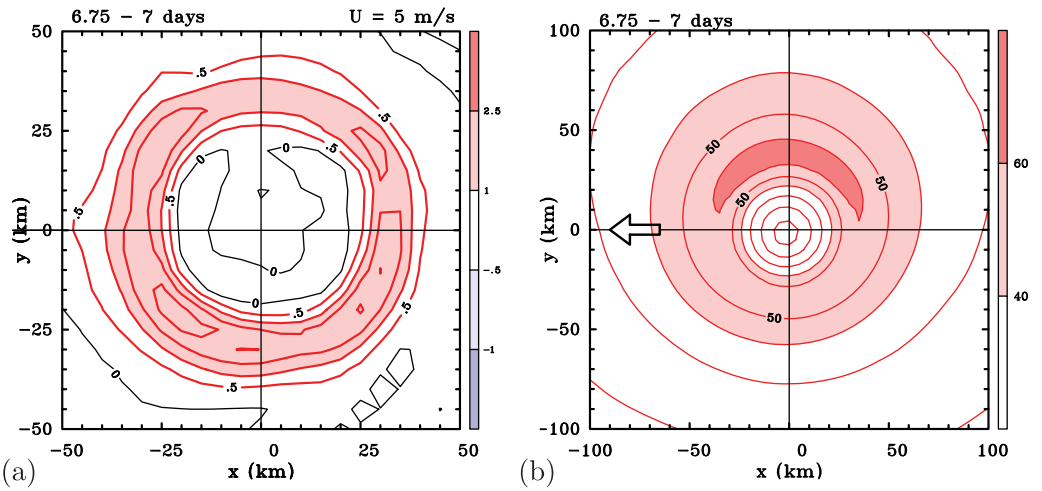

Figure 13. Calculation using the Gayno-Seaman boundary layer parameterization scheme with $U = 5$ m s^{-1}. (a) Pattern of vertical velocity, contour interval 0.5 m s^{-1}. Shading levels as indicated by label bar in m s^{-1}. Positive velocities (solid contours, pink, and red shading), negative velocities (dashed lines, light, and dark blue shading), and zero contour (thin, solid, and black). (b) Pattern of total wind speed at 850 mb in an Earth-relative frame averaged every 15 min during the period 6.75 and 7 days. Contour interval: thin contours 10 m s^{-1}. Values between 40 and 60 m s^{-1} shaded light red, values exceeding 60 m s^{-1} shaded red. The arrow indicates the direction of vortex motion.

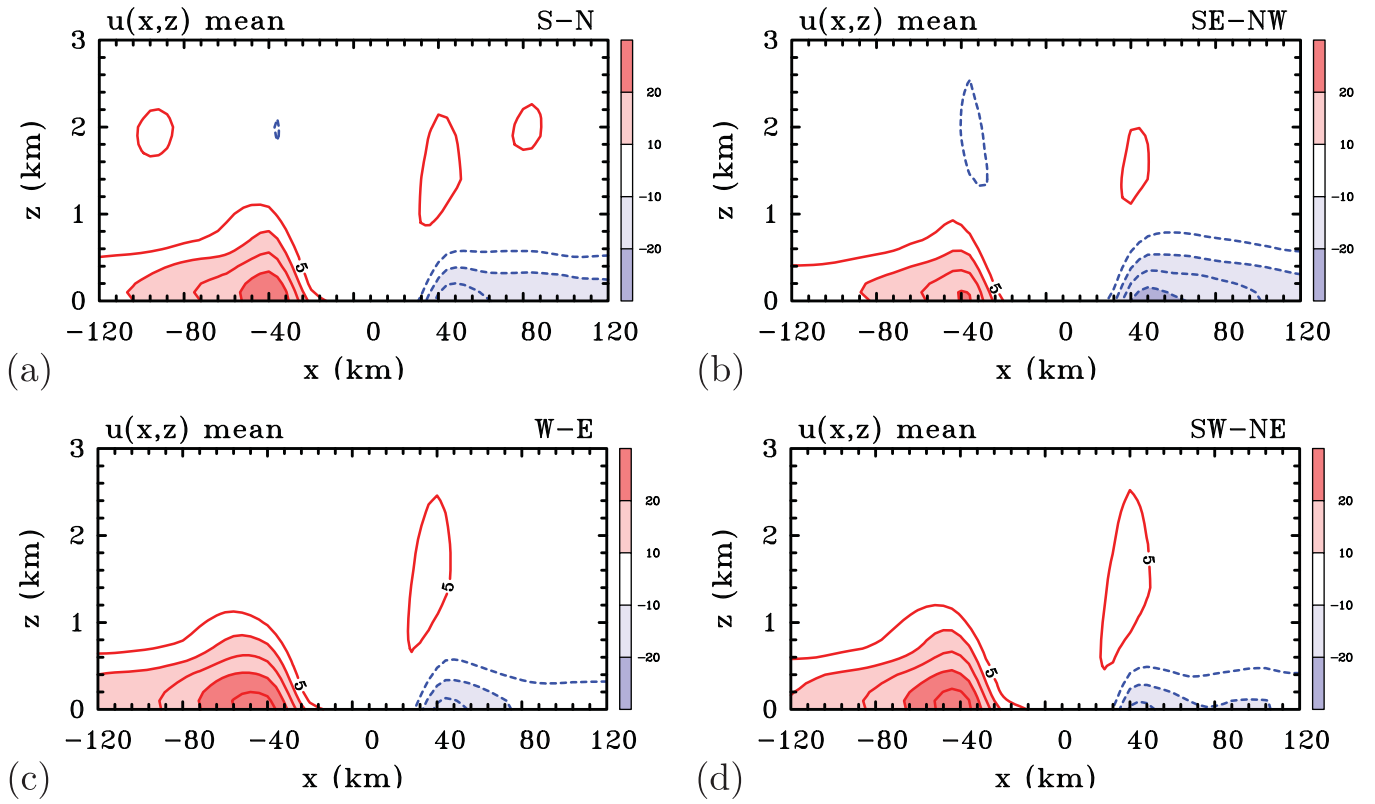

Figure 14. Height-radius cross sections showing isotachs of the wind component in different compass directions (x) in the comoving frame. The data are for the control calculation with $U = 5$ m s^{-1} and with the Gayno-Seaman boundary layer scheme, and are averaged every 15 min during the period 6.75 and 7 days. (a) South to north, (b) southeast to northwest, (c) west to east, (d) southwest to northeast. Contour interval: 5 m s^{-1}. Positive contours solid/red, negative contours dashed/blue. Shading levels as indicated on the label bar.

than the maximum found so far in observations suggesting that this scheme may be somewhat too diffusive. (As far as we are aware, the first observational estimates for this quantity are those analyzed from flight-level wind measurements at an altitude of about 500 m in Hurricanes Allen (1980) and Hugo (1989) by *Zhang et al.* [2011b]. In Hugo, maximum K-values were about 110 m^2 s^{-1} beneath the eyewall, where the near-surface wind speeds were about 60 m s^{-1}, and in Allen they were up to 74 m^2 s^{-1}, where wind speeds were about 72 m s^{-1}. More recently, *Zhang and Montgomery* [2012] obtained values of vertical diffusivity for Category 5 Hurricane David (1979) that are comparable to these values and obtained estimates of horizontal diffusivity for Hurricanes Hugo (1989), Allen (1980), and David (1979) in the boundary layer also. An additional paper by *Zhang and Drennan* [2012] used the CBLAST data in the rainband region of the hurricanes Fabian (2003), Isabel (2003), Frances (2004), and Jeanne (2004) to obtain vertical profiles of the vertical diffusivity with comparable, but somewhat weaker values to the values found by *Zhang et al.* [2011b]. In summary, we now have estimates of vertical diffusivity from seven different storms.)

Figure 12 compares the evolution of the maximum total wind speed at 850 mb for this case with that in the control calculation for $U = 5$ m s^{-1} and with that for the corresponding ensemble mean. As expected from the results of *Smith and Thomsen* [2010], the use of this scheme leads to a reduced intensification rate and a weaker vortex in the mature stage. However, as shown in Figure 13, the patterns of the wind and vertical velocity asymmetries are similar to those with the bulk scheme (e.g., compare Figure 13a with Figure 8f). Of course, the maxima of the respective fields are weaker. The same remarks apply also to the vertical cross sections of radial inflow shown in Figure 14. As in the corresponding calculation with the bulk scheme, the deepest and strongest inflow occurs on the downstream (western) side of the vortex and the weakest is on the upstream side (compare the plots in Figure 14 with the corresponding Figures 10c–10f). More generally, the inflow is strongest in the sector from northwest to south and weakest in that from southeast to north, but the magnitudes are smaller than with the bulk scheme.

7. Conclusions

We have presented an analysis of low-level flow asymmetries in the prototype problem for the intensification of a moving tropical cyclone using a three-dimensional, convection-permitting numerical model. The problem considers the evolution of an initially dry, axisymmetric vortex in hydrostatic and gradient wind balance, embedded in a uniform zonal flow on an *f*-plane. The calculations were designed to examine, using as simple a convection-permitting model as possible, the hypothesized effects of a uniform flow on the intensification, structural evolution, and mature intensity of a tropical cyclone. The calculations naturally complement those of *Nguyen et al*. [2008], who examined the processes of tropical-cyclone intensification in a quiescent environment from an ensemble perspective, and they provide a bridge between this problem and the intensification problem in vertical shear over a deep tropospheric layer. In particular, the paper addresses three outstanding basic questions concerning the effects of moist convection on the azimuthal flow asymmetries.

The first question is: does the imposition of a uniform flow lead to an organization of the inner-core convection making its distribution more predictable compared with the case of a quiescent environment? The answer to this question is a qualified yes. For the relatively strong vortices mostly studied here, the effect is pronounced only for background flow speeds larger than about 7 m s^{-1}. In such cases, we found that the time-averaged vertical velocity field at 850 mb during the last 6 h of the calculations has a vortex-scale maximum at about 45° to the left of the vortex motion vector. This maximum survives also in an ensemble mean of calculations in which the initial low-level moisture field is perturbed. Therefore, we conclude that this maximum is a robust feature and neither a transient one nor a property of a single realization associated with a particular mesoscale convective feature. In an Earth-relative frame, the total wind speed has a maximum in the forward right quadrant, a feature that survives also in the ensemble mean calculation. In the comoving frame, this maximum lies to the left of the motion vector in the ensemble mean. The low-level asymmetric wind structure found above remains unaltered when the more sophisticated, but more diffusive Gayno-Seaman scheme is used to represent the boundary layer, suggesting that our results are not overly sensitive to the boundary layer scheme used.

The second question is: to what extent do our results corroborate with those of previous theoretical investigations? A useful metric for comparing the results is via the vortex-scale pattern of vertical velocity at the top of the boundary layer. We find that the direction of the maximum vertical velocity is about 45° to the left of that predicted by Shapiro's nonlinear model [*Shapiro*, 1983], where the maximum is in the direction of motion. This difference may have consequences for the interpretations of observations, since Shapiro's results are frequently invoked as a theoretical benchmark for characterizing the boundary layer-induced vertical motion [e.g., *Corbosiero and Molinari*, 2003, p. 375]. The reason for the difference may be attributed, at least in part, to the fact that in our calculations, the vortex flow above the boundary layer is determined as part of a full solution for the flow and not prescribed. Looked at in another way, if the asymmetric pattern of vertical motion at the top of the boundary layer predicted by Shapiro's theory does lead to an asymmetry in the envelope of convection, the asymmetric flow induced by this envelope will modify the pattern of horizontal flow at the top of the boundary layer, thereby altering the structure of ascent induced by the boundary layer at its top and so on. Despite the inevitable existence of this coupling process, we would argue that Shapiro's nonlinear model provides an acceptable zero-order description of the boundary layer asymmetries that survive the transient effects of deep convection.

The third question is: how well do the findings compare with recent observations of boundary layer flow asymmetries in translating storms by *Kepert* [2006a, 2006b] and *Schwendike and Kepert* [2008]? We found that vertical cross sections of the 6 h averaged, storm-relative, tangential wind component in the lowest 3 km during the mature stage show a slight tendency for the maximum tangential wind component to become lower in altitude with decreasing radius as the radius of the maximum tangential wind is approached. Moreover, the storm-relative maximum tangential wind speed occurs on the left (i.e., southern) side of the storm as is found in the observations reported in the foregoing papers. Similar cross sections of the radial wind component show that the strongest and deepest inflow occurs in the sector from northwest to southwest (for a storm moving westward) and the weakest and shallowest inflow in the sector southeast to east, consistent also with the observations.

The ensemble calculations show that an increase in the background flow leads to a slight reduction in the intensification rate and to a weaker storm after 7 days. The reduction in mature intensity is on the order of

10 m s^{-1} from zero background flow to one of 12.5 m s^{-1}, although there are a few times when the reduction in intensity with background flow speed does not vary monotonically. The results on intensity reduction are in some sense consistent with those of the observational study of northwest Pacific storms by *Zeng et al*. [2007], who found that the most intense tropical cyclones and those with the most rapid intensification rates occur in this speed range when there is relatively weak vertical shear. In particular, they noted that "generally the intensification rate . . . increases with decreasing translation speed . . .," but their data fall short of showing a clear one-to-one relationship between intensity and translation speed.

Acknowledgments

G.L.T. and R.K.S. were supported in part by grant SM 30/23-1 from the German Research Council (DFG). R.K.S. is supported also by the Office of Naval Research Global under grant N62909-15-1-N021. M.T.M. acknowledges the support of NSF grants AGS-0733380 and NSF AGS-0851077 and NASA grants NNH09AK561 and NNG09HG031. The views expressed herein are those of the authors and do not represent sponsoring agencies or institutions. The data used in this paper can be accessed by e-mailing the second author at: rogerksmith@online.de.

References

Black, P. G., E. A. D'Asoro, W. M. Drennan, J. R. French, P. P. Niller, T. B. Sanford, E. J. Terril, E. J. Walsh, and J. A. Zhang (2007), Air-sea exchange in hurricanes: Synthesis of observations from the coupled boundary layer air-sea transfer experiment, *Bull. Am. Meteorol. Soc.*, *88*, 357–374.

Braun, S. A., and W.-K. Tao (2000), Sensitivity of high-resolution simulations of Hurricane Bob (1991) to planetary boundary layer parameterizations, *Mon. Weather Rev.*, *128*, 3941–3961.

Bryan, G. H., and R. Rotunno (2009), Evaluation of an analytical model for the maximum intensity of tropical cyclones, *J. Atmos. Sci.*, *66*, 3042–3060.

Bui, H. H., R. K. Smith, M. T. Montgomery, and J. Peng (2009), Balanced and unbalanced aspects of tropical-cyclone intensification, *Q. J. R. Meteorol. Soc.*, *135*, 1715–1731.

Callaghan, J., and R. K. Smith (1998), The relationship between maximum surface wind speeds and central pressure in tropical cyclones, *Aust. Meteorol. Mag.*, *47*, 191–202.

Corbosiero, K. L., and J. Molinari (2002), The effects of vertical wind shear on the distribution of convection in tropical cyclones, *Mon. Weather Rev.*, *130*, 2110–2123.

Corbosiero, K. L., and J. Molinari (2003), The relationship between storm motion, vertical wind shear, and convective asymmetries in tropical cyclones, *J. Atmos. Sci.*, *60*, 366–376.

Dudhia, J. (1993), A non-hydrostatic version of the Penn State/NCAR mesoscale model: Validation tests and simulation of an Atlantic cyclone and cold front, *Mon. Weather Rev.*, *121*, 1493–1513.

Frank, W. M., and E. A. Ritchie (1999), Effects of environmental flow on tropical cyclone structure, *Mon. Weather Rev.*, *127*, 2044–2061.

Frank, W. M., and E. A. Ritchie (2001), Effects of vertical wind shear on the intensity and structure of numerically simulated hurricanes, *Mon. Weather Rev.*, *129*, 2249–2269.

Grell, G. A., J. Dudhia, and D. R. Stauffer (1995), A description of the fifth generation Penn State/NCAR mesoscale model (MM5), *NCAR Tech. Note NCAR/TN-398+STR*, pp. 138, Nat. Cent. Atmos. Res., Boulder, Colo.

Jones, S. C. (1995), The evolution of vortices in vertical shear. Part I: Initially barotropic vortices, *Q. J. R. Meteorol. Soc.*, *121*, 821–851.

Jones, S. C. (2000), The evolution of vortices in vertical shear. III: Baroclinic vortices, *Q. J. R. Meteorol. Soc.*, *126*, 3161–3186.

Jordan, C. L. (1958), Mean soundings for the West Indies area, *J. Meteorol.*, *15*, 91–97.

Kepert, J. D. (2001), The dynamics of boundary layer jets within the tropical cyclone core. Part I: Linear theory, *J. Atmos. Sci.*, *58*, 2469–2484.

Kepert, J. D. (2006a), Observed boundary-layer wind structure and balance in the hurricane core. Part I. Hurricane Georges, *J. Atmos. Sci.*, *63*, 2169–2193.

Kepert, J. D. (2006b), Observed boundary-layer wind structure and balance in the hurricane core. Part II. Hurricane Mitch, *J. Atmos. Sci.*, *63*, 2194–2211.

Kepert, J. D. (2012), Choosing a boundary-layer parameterisation for tropical cyclone modelling, *Mon. Weather Rev.*, *140*, 1427–1445.

Kepert, J. D., and Y. Wang (2001), The dynamics of boundary layer jets within the tropical cyclone core. Part II: Nonlinear enhancement, *J. Atmos. Sci.*, *58*, 2485–2501.

McIntyre, M. E. (1993), Isentropic distributions of potential vorticity and their relevance to tropical cyclone dynamics, in *Tropical Cyclone Disasters: Proceedings of ICSU/WMO International Symposium*, edited by J. Lighthill et al., pp. 143–156, Peking Univ. Press, Beijing.

Montgomery, M. T., M. M. Bell, S. D. Aberson, and M. L. Black (2006), Hurricane isabel (2003): New insights into the physics of intense storms. Part I mean vortex structure and maximum intensity estimates, *Bull. Am. Meteorol. Soc.*, *87*, 1335–1348.

Nguyen, V. S., R. K. Smith, and M. T. Montgomery (2008), Tropical-cyclone intensification and predictability in three dimensions, *Q. J. R. Meteorol. Soc.*, *134*, 563–582.

Powell, M. D. (1982), The transition of the Hurricane Frederic boundary layer wind field from the open gulf of Mexico to landfall, *Mon. Weather Rev.*, *110*, 1912–1932.

Raymond, D. J. (1992), Nonlinear balance and potential-vorticity thinking at large Rossby number, *Q. J. R. Meteorol. Soc.*, *118*, 987–1015.

Reasor, P. D., and M. T. Montgomery (2015), Evaluation of a heuristic model for tropical cyclone resilience, *J. Atmos. Sci.*, *72*, 1765–1782.

Reasor, P. D., M. T. Montgomery, and L. D. Grasso (2004), A new look at the problem of tropical cyclones in vertical shear flow: Vortex resiliency, *J. Atmos. Sci.*, *61*, 3–22.

Riemer, M., M. T. Montgomery, and M. E. Nicholls (2010), A new paradigm for intensity modification of tropical cyclones: Thermodynamic impact of vertical wind shear on the inflow layer, *Atmos. Chem. Phys.*, *10*, 3163–3188.

Riemer, M., M. T. Montgomery, and M. E. Nicholls (2013), Further examination of the thermodynamic modification of the inflow layer of tropical cyclones by vertical wind shear, *Atmos. Chem. Phys.*, *13*, 327–346.

Rogers, R., S. Lorsolo, P. Reasor, J. Gamache, and F. Marks (2012), Multiscale analysis of tropical cyclone kinematic structure from airborne Doppler radar composites, *Mon. Weather Rev.*, *140*, 77–99.

Schwendike, J., and J. D. Kepert (2008), The boundary layer winds in Hurricane Danielle (1998) and Isabel (2003), *Mon. Weather Rev.*, *136*, 3168–3192.

Shafran, P. C., N. L. Seaman, and G. A. Gayno (2000), Evaluation of numerical predictions of boundary layer structure during the Lake Michigan ozone study, *J. Appl. Meteorol.*, *39*, 3168–3192.

Shapiro, L. J. (1983), The asymmetric boundary layer flow under a translating hurricane, *J. Atmos. Sci.*, *40*, 1984–1998.

Shin, S., and R. K. Smith (2008), Tropical-cyclone intensification and predictability in a minimal three-dimensional model, *Q. J. R. Meteorol. Soc.*, *134*, 337–351.

Smith, R. K. (2006), Accurate determination of a balanced axisymmetric vortex, *Tellus, Ser. A*, *58*, 98–103.

Smith, R. K., and M. T. Montgomery (2013), On the existence of the logarithmic surface layer in the inner core of hurricanes, *Q. J. R. Meteorol. Soc.*, *140*, 72–81.
Smith, R. K., and G. L. Thomsen (2010), Dependence of tropical-cyclone intensification on the boundary layer representation in a numerical model, *Q. J. R. Meteorol. Soc.*, *136*, 1671–1685.
Smith, R. K., W. Ulrich, and G. Sneddon (2000), On the dynamics of hurricane-like vortices in vertical shear flows, *Q. J. R. Meteorol. Soc.*, *126*, 2653–2670.
Smith, R. K., M. T. Montgomery, and S. V. Nguyen (2009), Tropical cyclone spin up revisited, *Q. J. R. Meteorol. Soc.*, *135*, 1321–1335.
Smith, R. K., G. Kilroy, and M. T. Montgomery (2015), Why do model tropical cyclones intensify more rapidly at low latitudes?, *J. Atmos. Sci.*, *72*, 1783–1804.
Vogl, S., and R. K. Smith (2009), Limitations of a linear model for the hurricane boundary layer, *Q. J. R. Meteorol. Soc.*, *135*, 839–850.
Weckwerth, T. (2000), The effect of small-scale moisture variability on thunderstorm initiation, *Mon. Weather Rev.*, *128*, 4017–4030.
Williams, G. J. (2015), The effects of vortex structure and vortex translation on the tropical cyclone boundary layer wind field, *J. Adv. Model. Earth Syst.*, *7*, 188–214, doi:10.1002/2013MS000299.
Zeng, Z., Y. Wang, and C. C. Wu (2007), Environmental dynamical control of tropical cyclone intensity—An observational study, *Mon. Weather Rev.*, *135*, 38–59.
Zhang, J., W. M. Drennan, P. B. Black, and J. R. French (2009), Turbulence structure of the hurricane boundary layer between the outer rainbands, *J. Atmos. Sci.*, *66*, 2455–2467.
Zhang, J. A., and W. A. Drennan (2012), An observational study of vertical eddy diffusivity in the hurricane boundary layer, *J. Atmos. Sci.*, *69*, 3223–3236.
Zhang, J. A., and M. T. Montgomery (2012), Observational estimates of the horizontal eddy diffusivity and mixing length in the low-level region of intense hurricanes, *J. Atmos. Sci.*, *69*, 1306–1316.
Zhang, J. A., and E. Ulhorn (2012), Hurricane sea surface inflow angle and an observation-based parametric model, *Mon. Weather Rev.*, *10*, 3587–3605.
Zhang, J. A., R. F. Rogers, D. S. Nolan, and F. D. Marks (2011a), On the characteristic height scales of the hurricane boundary layer, *Mon. Weather Rev.*, *139*, 2523–2535.
Zhang, J. A., F. D. Marks, M. T. Montgomery, and S. Lorsolo (2011b), An estimation of turbulent characteristics in the low-level region of intense Hurricanes Allen (1980) and Hugo (1989), *Mon. Weather Rev.*, *139*, 1447–1462.
Zhang, J. A., R. F. Rogers, D. S. Nolan, and F. D. Marks (2013), Asymmetric hurricane boundary layer structure from dropsonde composites in relation to the environmental vertical wind shear, *Mon. Weather Rev.*, *141*, 3968–3983.